



Underlying limitations behind impedance rise and capacity fade of single crystalline Ni-rich cathodes synthesized via a molten-salt route

Luqman Azhari^a, Zifei Meng^a, Zhenzhen Yang^b, Guanhui Gao^c, Yimo Han^c, Yan Wang^{a,*}

^a Department of Materials Science and Engineering, Worcester Polytechnic Institute, 100 Institute Road, Worcester, MA, 01609, USA

^b Chemical Science and Engineering Division, Argonne National Laboratory, 9700 S. Cass Avenue, Lemont, IL, 60439, USA

^c Rice Electron Microscopy Center, Rice University, 6100 Main Street, Houston, TX, USA, 77005

ARTICLE INFO

Keywords:

Li-ion battery
NMC
LiNi_{0.8}Mn_{0.1}Co_{0.1}O₂
Single-crystal
Intragranular fracture

ABSTRACT

Layered oxide LiNi_xMn_yCo_zO₂ (NMC) cathodes are often synthesized as polycrystalline secondary particles. Due to intergranular fracture stemming from volume changes of randomly oriented primary particles during charge/discharge, the synthesis of larger single-crystalline cathodes is of high interest. In this work, molten salt assisted growth of micron-sized Ni-rich crystals is achieved with excellent crystallinity, low cation mixing, and negligible impurities. However, electrochemical performance is compromised by high surface reactivity resulting in decomposition of electrolyte and subsequent formation of a thick CEI layer. While intergranular fracture is eliminated, planar gliding and severe intragranular fracture along the (003) plane occurs in the high voltage region within the first few cycles and is associated primarily with H2 to H3 structural transitions. In addition, H2 to H3 transitions are highly irreversible with cyclic voltammograms revealing polarization growth within < 5 cycles. Subsequently, the single-crystalline material exhibited markedly reduced available capacity and enhanced capacity fade from sharp impedance growth compared to its polycrystalline counterpart. This work furthers a fundamental understanding into the limitations of single-crystalline Ni-rich cathodes, and the obstacles limiting the advantages offered by the single-crystalline morphology.

1. Introduction

Layered oxide nickel-rich NMC cathodes composed of the composition LiNi_xMn_{1-x-y}Co_yO₂, with $x > 0.6$, are expected to be implemented for next generation commercial lithium-ion batteries. Specifically, “NMC811”, with the composition of LiNi_{0.8}Mn_{0.1}Co_{0.1}O₂, is of significant interest; with a high practical specific capacity of 200mAh/g, low cost due to decreased cobalt content, and high discharge potential of 3.8 V (vs Li/Li⁺), and it has the potential to meet the rising energy requirements for electric vehicles, drones, and personal electronics of the near future [1–4]. However, increasing the nickel content of NMC cathodes to this extent poses significant obstacles that need to be addressed, specifically regarding calendar life and safety. Ni-rich cathode materials can suffer from capacity loss from transition metal (TM) migration to lithium sites during cycling [4–7], gas evolution from Ni⁴⁺ reactivity with conventional electrolytes in the highly charged state [8], surface reconstruction from the layered R-3m to spinel and highly resistive rock-salt phases [9,10], transition metal dissolution and electrode cross-talk [11,12], and intergranular cracking from large anisotropic

volume changes during high levels of delithiation [10]. Most of these issues are exacerbated when using higher cutoff voltages above 4.3 V due to the high valence state of Ni⁴⁺ and occurrence of the H2 to H3 transition around this region [13].

Of the various degradation mechanisms listed above, intergranular cracking has been highlighted as a major issue that should be addressed [14–16]. Intergranular cracking, also known as “electrochemical shock,” typically occurs during high voltage cycling and is attributed to large and sudden anisotropic volume changes in the *c* lattice parameter associated with the H2 to H3 transition [17]. In-situ XRD data in other studies involving Ni-rich NMC have well documented an expansion in the *c* lattice parameter during delithiation until 4.3 V, after which a sudden contraction and shrinkage of the crystal lattice along the (003) direction occurs [13]. This mechanism is due to the gradual electronic repulsion of the oxygen slabs and decreased shielding from Li⁺ ions during initial delithiation, followed by collapse of the layer under higher state of charge from increased Ni–O covalency and loss of Li pillaring [13,18]. Subsequent intergranular fracture can lead to the development of microcracks, which can expose the interior of the particle to

* Corresponding author.

E-mail address: yanwang@wpi.edu (Y. Wang).

<https://doi.org/10.1016/j.jpowsour.2022.231963>

Received 25 June 2022; Received in revised form 4 August 2022; Accepted 8 August 2022
0378-7753/© 20XX

electrolyte penetration, leading to increased levels of surface-initiated degradation mechanisms, subsequent increase in impedance, and electrical disconnection in severe cases. This degradation mechanism is especially prevalent in NMC powders synthesized through conventional high-throughput coprecipitation methods, where the final products are secondary particles 8–16 μm in diameter and composed of many randomly oriented individual primary particles 100–200 nm in size [19]. In these polycrystalline materials, intergranular fracture is well documented and exacerbated when increasing the nickel content or upper cutoff voltage [17,18,20,21].

To mitigate or completely remove the impact of intergranular fracture, an increasingly popular method is to synthesize powders composed of large single crystals of NMC instead of polycrystalline secondary particles. To achieve this, previous studies have utilized a variety of different synthesis methods, ranging from molten salt flux growth [22–24], high energy ball milling [25–27], chemical etching of secondary particles [28], and high temperature sintering [29]. Different particle sizes and morphologies can be obtained based on a variety of experimental parameters such as sintering temperature, flux, oxygen and lithium chemical activity, and time [30]. Successful growth of single crystalline NMC622 was demonstrated using a combination of molten salt and high temperature synthesis [22,29]. Dahn et al. have also demonstrated a variety of single crystal NMC532 and NMC622 cathodes using high temperature calcination combined with grinding and sieving, although electrochemical performance was subpar compared to their polycrystalline analogues [25,31,32]. To date, single crystal NMC has been shown to have superior cycling performance due to the absence of cracking [22] as well as reduced electrode crosstalk from higher surface to volume ratio [33]. In addition, Zhao et al. demonstrated that single crystal NMC622 pouch cells exhibited significantly reduced transition metal dissolution and gas evolution compared to polycrystalline counterparts [34]. However, it is even more challenging to synthesize Ni-rich single crystal cathodes such as NMC811 due to a generally lower optimum calcination temperature [35]. Increasing the calcination temperature is generally required to facilitate solid state growth, but also facilitates the formation of undesirable NiO and excessive cation mixing [35]. While some works have demonstrated successful synthesis of Ni-rich single crystal cathodes, they require the use of ball milling or other mechanical pulverization of agglomerates [27,36].

In this work, we demonstrate synthesis of single-crystalline Ni-rich cathode powders $\sim 1\text{--}2\ \mu\text{m}$ in size using a combination of high temperature synthesis, excess Li, and molten salt flux. The resulting cathode powders exhibit excellent crystallinity, with lower levels of cation mixing and increased $\text{Ni}^{3+}/\text{Ni}^{2+}$ surface compositions. The use of molten salt flux reduces size distribution inhomogeneity and agglomeration, with the excess molten salt flux easily washed away using deionized water. Despite the crystallinity and surface quality of the initial material, we demonstrate that Ni-rich single crystalline cathodes with dominant (012) facets exhibit higher surface reactivity resulting in the formation of a thicker cathode electrolyte interphase. The H2 to H3 transition in the high voltage is shown to be much more irreversible compared to the polycrystalline counterpart, with increasing polarization and intragranular cracking along the weaker basal plane observed within the first few cycles. Lastly, rapid increases in charge transfer overpotentials occur beyond moderate levels of delithiation, which is not observed in the polycrystalline counterpart. Overall, these mechanisms limit the reversible capacity and long-term stability of the single-crystalline Ni-rich cathode, and will require further tuning through dopants or morphology control to become competitive with traditional polycrystalline cathodes.

2. Experimental methods

2.1. Synthesis of polycrystalline NMC811

To prepare polycrystalline NMC811 cathodes (“PC811”), spherical hydroxide precursors are first synthesized using a coprecipitation procedure based on a prior study [37]. A solution of transition metal sulfates in the targeted ratio (Ni:Mn:Co = 8:1:1) is added dropwise into a stirring glass jacketed reactor under nitrogen atmosphere. Ammonia is added to the reactor to reduce the coprecipitation reaction rate as a chelating agent. The pH is maintained at 11 ± 0.1 using a solution of sodium hydroxide, which also functions as the precipitating agent/counter anion. After a fixed reaction time, the hydroxide product is collected, rinsed with deionized water, and dried thoroughly to remove excess water. The obtained powder is then mixed thoroughly with lithium hydroxide in a 1:1.05 M ratio to account for lithium volatilization and calcined at 450 $^{\circ}\text{C}$. The powder is then removed and gently ground again to homogenize possible lithium concentration irregularities, followed by a subsequent calcination at 775 $^{\circ}\text{C}$ under flowing oxygen.

2.2. Synthesis of single-crystalline NMC811

Single crystalline NMC811 (“SC811”) is synthesized via a molten-salt method using the same hydroxide precursors described in the previous section. The hydroxide powder is mixed with 50 mol% excess lithium hydroxide and a eutectic mixture of lithium sulfate and sodium sulfate (0.62–0.38) [38]. The eutectic composition has a melting point of approximately 580 $^{\circ}\text{C}$, and sulfate-based fluxes are effective for the dissolution of oxides compared to other potential salt systems [38–40]. In a previous study on the molten salt growth of lead magnesium niobates, the oxide solubility using a $\text{Li}_2\text{SO}_4\text{--Na}_2\text{SO}_4$ mixture was nearly one order of magnitude higher than that of chloride flux [40]. It is understood that growth occurs via a dissolution-recrystallization mechanism which dissolves smaller oxide particles to facilitate the growth of larger particles through Ostwald ripening processes, with the molten flux allowing for faster mass transport than simple solid-state growth [24]. The presence of the larger alkali Na^+ ions in the flux composition is also critical in molten salt growth by being more effective solvating O^{2-} anions than Li^+ [41].

The mixture is calcined using a two-step high temperature/low temperature profile similar to a previous study [29]; the sample is subject to a shorter calcination at 900 $^{\circ}\text{C}$ for 2 h, followed by a longer 13-h soak time at 775 $^{\circ}\text{C}$ to ensure good crystallinity. The collected sample is typically in the form of a “brick,” which is then ground gently, followed by ultrasonic washing in deionized water to remove the water-soluble salts. The resulting powder is then dried at 100 $^{\circ}\text{C}$ in a vacuum oven for several hours, followed by an annealing step at 650 $^{\circ}\text{C}$ for 5 hrs under flowing oxygen, which is necessary to recover surface damage from the washing process and improve electrochemical performance [22–24,42].

2.3. Electrode/half-cell fabrication

To form electrodes, PC811 or SC811 powder is mixed with Super C65 carbon black as a conductive additive and PVDF dissolved in NMP (6 wt%) as a binder. The slurry is composed of 80 wt% of active material, 10 wt% carbon black, and 10 wt% PVDF. The resulting slurry is cast onto a 15 μm thick Al foil using a 150 μm doctor blade and dried at 70 $^{\circ}\text{C}$ in air for several hours until the surface appears dry, followed by drying overnight in a vacuum oven at 120 $^{\circ}\text{C}$ to remove residual solvents and possible moisture. Afterwards the electrode is calendered to an approximate total thickness of 35–40 μm , punched into 12 mm discs, and assembled into 2032-coin cells in an argon-filled glovebox with lithium metal as the anode, 1.0 M LiPF_6 in EC/EMC (3:7 wt ratio)

as the electrolyte, and a Celgard separator. Active mass loadings are calculated to be in the range of 3.5–4.3 mg/cm².

3. Characterization methods

X-ray diffraction (XRD) profiles were obtained using a PANalytical Empyrean X-ray Diffractometer (Cu K α , $\lambda = 1.5409 \text{ \AA}$ radiation source, and step size of 0.0167°/step). Analysis of the XRD profiles was performed using Rietveld refinement technique via Fullprof Suite to determine crystallographic lattice parameters, degree of cation mixing, and $I_{(003)}/I_{(104)}$ ratios, using R-3m space group as the structural reference. Surface morphology, qualitative chemical information, and elemental distribution of the cathode powders were examined using SEM and EDS analysis via a JEOL JSM-7000F SEM at 10 kV accelerating voltage. Chemical compositions were determined through ICP-OES via a PerkinElmer Optima 8000. High-resolution transmission electron microscopy (HRTEM) is performed using a Titan cubed Themis 300 at 300 kV, with EDS mapping performed in STEM mode. X-ray photoelectron spectra (XPS) analysis is performed via a PHI 5000 VersaProbe II system (Physical Electronics). Individual scans across the Li 1s, O 1s, C 1s, Co 2p₃, Mn 2p₃, Ni 2p₃, and F 1s binding energies were collected at a pass energy of 23.50 eV and electron escape angle of 45° to the sample plane. Ar-ion milling for 2 min at 4 kV was utilized to remove the surface material and probe subsurface regions less than ~100 nm from the surface. Relevant XPS spectra were deconvoluted and fitted using XPS-Peak software to examine the surface oxidation states of the powder in the as-synthesized state and electrodes taken from disassembled cells after 100 cycles.

Galvanostatic charge/discharge cycling was conducted at ambient room temperature on a LANDT CT2001A from 2.8 to 4.5 V at a C/2 rate. Electrochemical performance was also examined under different current loads of C/10, C/5, C/2, 1C, 2C, 3C, and C/10. Cyclic voltammetry (CV) and electrochemical impedance spectroscopy (EIS) were obtained using a Bio-logic SAS VMP3 multi-channel Potentiostat maintained at 30 °C. CV and EIS data were obtained for cells before and after

cycling. CV profiles were obtained using a scan rate of 0.1 mV/s from a voltage range of 2.8–4.5 V. EIS was obtained using a 10 mV sinusoidal amplitude from 1 MHz to 20 mHz. Cells were subjected to a constant voltage hold at the desired SOC/voltage for approximately 2 h before EIS analysis to ensure the electrode was at the desired SOC. Galvanostatic intermittent titration technique (GITT) was utilized to determine SOC dependent lithium diffusion coefficients and polarization and was conducted using a C/10 current pulse for 0.5 hrs, followed by 1.5 hrs of resting time. GITT measurements for each sample were collected across one full charge cycle and discharge cycle.

4. Results and discussion

4.1. Morphology and crystallinity

The morphology of PC811 and SC811 are examined with SEM in Fig. 1a–d and demonstrates the contrasting size and shape distribution between the polycrystalline and single crystalline NMC811. Like previous works, PC811 is composed of spherical secondary particles ~8–10 μm in diameter and consisting of elongated block-like primary particles ~50–200 nm in size [43]. SC811 is composed primarily of 1–2 μm crystals with well-defined facets. The cathode crystal shape is observed to be mostly composed of octahedral-shaped crystals which, based on DFT calculations for equilibrium shapes of NMC from a study by Zhu et al., is assumed to be enclosed mostly by (012) facets [30]. Such shapes are expected to form when sintering under high oxygen and lithium activity, which was achieved through use of excess Li and flowing oxygen conditions [30]. High temperature and excess Li were found to be necessary to synthesize single crystalline NMC811, as reducing the upper temperature to 825 °C was found to still retain the highly polycrystalline morphology [Fig. S1e].

The use of 10 mol% Li₂SO₄-Na₂SO₄ flux was sufficient in producing well separated single crystals with consistent size and shape, due to the solubility of oxides in sulfate molten salts [39]. Although SC811 samples synthesized without the use of molten salt flux still resulted in large

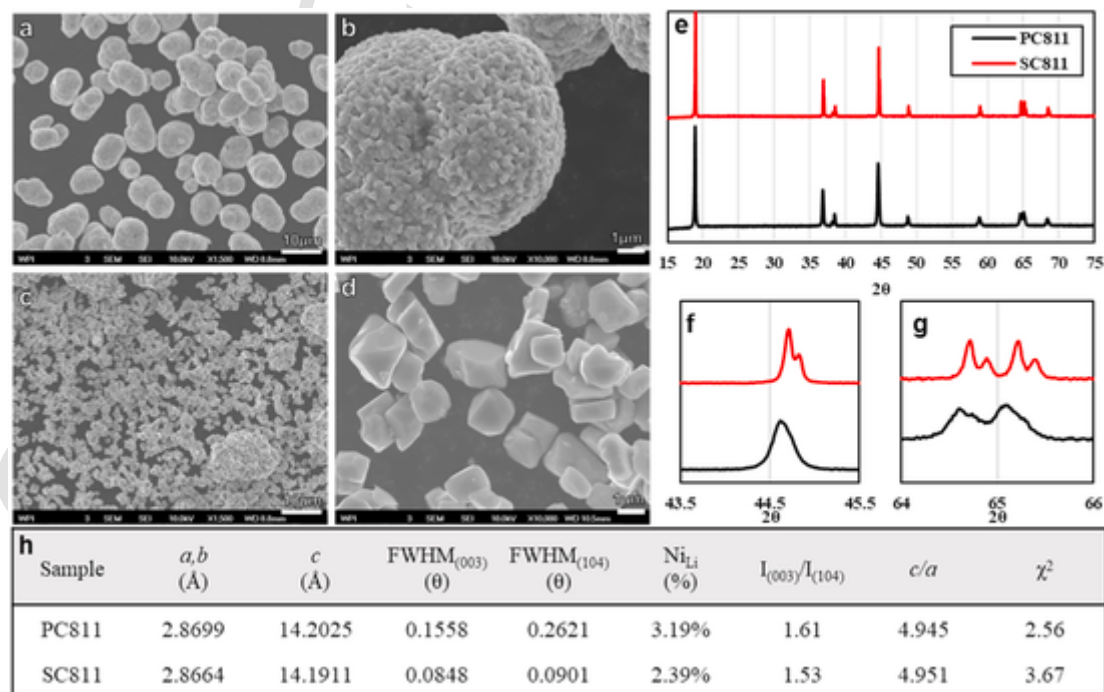


Fig. 1. SEM images of as-synthesized PC811 (a,b) and SC811 powders (c,d). SC811 powders are observed to form in octahedral shapes dominated by (001) and (012) surfaces, although other shapes are occasionally observed. (e) Powder XRD profiles for PC811 and SC811. (f,g) Selected 2θ ranges of the (104) and (108/110) peaks, respectively, demonstrating the smaller FWHM and well separated $K\alpha$ doublet peaks of SC811 compared to PC811. (h) Table of relevant crystallographic parameters, obtained from Rietveld Refinement of XRD profiles.

crystal sizes, the resulting powder exhibited severe agglomeration and wider particle size distribution due to the lack of molten salt flux [Figs. S1a–d]. This is also indicated from Fig. S2, where the d50 and specific surface area of single crystal samples prepared without sulfate flux is noticeably higher than that with 10 mol% sulfate flux, indicative of increased agglomeration and wider particle size distributions. It also is worth noting that increasing the excess LiOH is effective in reducing agglomeration and breaking apart secondary particles, as LiOH in excess will also function as a molten salt flux [Fig. S3]. An increase in the sulfate flux content to 50 mol% expectedly retains the well separated and narrower size distribution, demonstrated in Fig. S1f. However, the average size is noticeably reduced due to the increased diffusion length and oxide solvation. Therefore, by controlling the different variables of high temperature synthesis, excess Li, and molten salt flux type and concentration, 1–2 μm sized octahedral single crystals of NMC811 with narrow size distribution and less agglomeration could be obtained.

Both PC811 and SC811 exhibit no noticeable impurity phases, shown in the selected XRD profiles in Fig. 1e–g. Both XRD patterns display the typical characteristic peaks of the hexagonal $\alpha\text{-NaFeO}_2$ layered structure of R-3m space group, with excellent crystallinity as made evident by the clear splitting of the (006)/(102) and (108)/(110) peaks [28]. SC811 exhibits superior long-range ordering due to the larger single-crystalline nature; the full-width half maximum (FWHM) of selected peaks are noticeable smaller, consistent with Scherrer relationship between crystallite size and peak width [44]. Moreover, doublet peaks can be observed due to reflections from both Cu $K\alpha_1$ and $K\alpha_2$ wavelengths, while such resolution cannot be observed in PC811 due to peak broadening. Both samples retain the expected composition based on ICP data in Table S1, with no lithium deficiency.

From the XRD refinement data in the table in Fig. 1h, SC811 exhibits slightly smaller lattice parameters compared to PC811. In addition, SC811 samples have noticeably lower cation mixing than PC811, with only 2.39% cation mixing in the Li layer compared to 3.19% for PC811. The decreased cation mixing implies less Ni^{2+} in the Li layer for SC811, which would also correspond to the slightly smaller lattice parameters. The low cation mixing is further indicated by the higher c/a ratio for SC811 and excellent (003)/(104) intensity ratios for both samples. While the (003)/(104) ratio for SC811 is slightly lower than PC811, despite the lower cation mixing determined through Rietveld refinement, this difference is attributed to the faceted nature of SC811 with the pre-

ferred orientation during sample packing likely influencing the (003) and (104) peak intensities. The lower cation mixing can be understood when considering that the flux-assisted process allows for enhanced transport of the metal cations, along with dissolution and recrystallization suppressing the amount of nickel ions settling into lithium sites under a sufficiently oxidizing atmosphere. Thus, the demonstrated synthesis method can achieve excellent crystallinity with low cation mixing. The addition of excessive amounts of sulfate flux results in a decline in crystallinity, as evidenced by the higher degree of cation mixing determined in Fig. S4 for samples prepared with 50 mol% sulfate flux.

4.2. Surface composition and structure

The surface composition and structure are probed using XPS and TEM techniques. Despite using sulfate fluxes containing sodium, no significant sodium, sulfur, or aluminum impurity can be detected for SC811 [Fig. S5], demonstrating the effectiveness of the water washing and annealing procedure to remove the soluble sulfate flux. As shown in Fig. 2a and b, the Ni 2p3 spectra can be deconvoluted into 4 peaks centered around 855.76, 854.6, 861, and 862.5 eV [45,46]. Contributions from Ni^{2+} and Ni^{3+} oxidation states correspond to peaks at 855.76 eV and 854.6 eV, respectively, while others represent satellite peaks. Ni^{2+} exists on the surface of Ni-rich NMC as the higher energy surface is sensitive to ambient conditions and lattice lithium can react with moisture and carbon dioxide to form a residual lithium layer along with a corresponding reduction of nickel at the surface/subsurface region. By comparing the integrated area for each peak, an estimate of the nickel valence state ~ 5 nm from the surface can be obtained. A higher fraction of Ni^{3+} is typically associated with better ordering, surface stability, and less cation mixing, as nickel should exist mostly in the 3+ oxidation state in pristine NMC811 [47,48]. As shown in the table in Fig. 2e of the areal contributions of individual peaks to the total integrated area, PC811 has a significantly higher percentage of Ni^{2+} (42.5%) compared to SC811 samples (9.5%), indicating a much more pristine surface structure for SC811 with less inherent surface reconstruction. It also suggests that cation mixing is easier to occur in PC811 samples than SC811 samples, which is consistent with XRD refinement results. For O1s spectra in Fig. 2c and d, there are two distinct peaks observed at positions of 531.9 and 529 eV [49]. The peak at 531.9 eV represents higher energy active oxygen (O_{active}), and the peak at 529.3 eV corre-

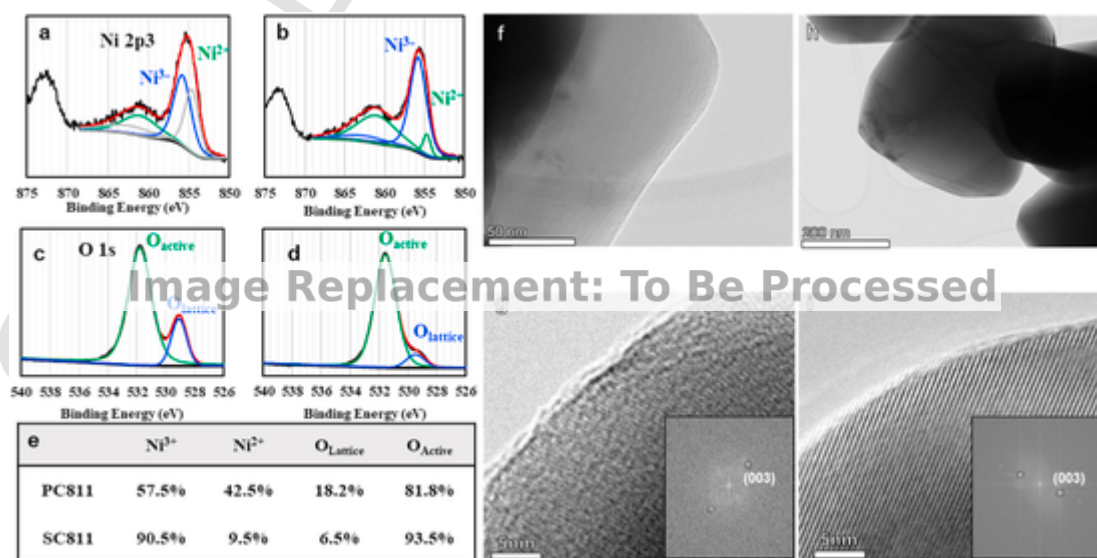


Fig. 2. Ni 2p3 and O1s binding energies for (a, c) PC811 and (b, d) SC811 as-synthesized powders, with deconvoluted peaks. A SC811 particle was prepared by FIB to obtain a cross section for EDS and for obtaining a sufficiently thin particle section (e) Contribution of deconvoluted peaks to the overall signal. HAADF and HRTEM imaging of a primary particle edge for (f,g) PC811 and (h,i) SC811. FFT patterns in the inset are both indexed to the (003) lattice fringes of the layered R-3m structure. FFT points are circled for clarity.

sponding to lattice-bonded oxygen (O_{lattice}) [49]. According to the table in Fig. 2e, the percentage of O_{lattice} in SC811 samples is moderately less than that in PC811 samples, indicating that there are more defects or broken bonds on the surface of SC811 samples, which may be a result of the more reactive (012) facets of the octahedral morphology. While the O_{active} is also considered to be present in the form of residual lithium such as Li_2CO_3 , XPS analysis and deconvolution of the carbon 1S binding energies indicate similar levels of carbonate content, indicating that the difference in O_{active} is attributed to the higher energy facets [Fig. S6]. This is also confirmed from the HAADF and HRTEM imaging of a particle edge for as-synthesized PC811 and SC811 samples in Fig. 2f–i, which show similar thicknesses of residuals along with clear lattice fringes. Cross sectional EDS mapping also verifies that transition metal distribution is homogenous across the entire particle, with no significant segregation [Fig. S7].

4.3. Electrochemical performance

While both SC811 and PC811 exhibit similar first coulombic efficiencies between 85 and 88% with similar voltage profiles and plateaus, SC811 suffers from a noticeably higher potential drop of 83 mV upon first discharge, compared to 40 mV for PC811 [Fig. 3a]. In addition, the first discharge capacity is noticeably lower at 199mAh/g vs 211 for PC811. Upon cycling at a C/2 rate, shown in Fig. 3b, the reversible capacity of SC811 drops even lower to around 160mAh/g with a capacity fade that is more severe compared to PC811, which was somewhat unexpected due to the intended improvement in regard to intergranular fracture.

The loss in accessible capacity is also observed at different rates of charge/discharge, with SC811 typically exhibiting a specific capacity 10–25mAh/g lower than its polycrystalline counterpart [Fig. 3c]. However, this is not the case for 5C, where it is observed that both samples exhibit the same reversible capacity of ~125mAh/g. When examining the individual capacity-voltage curves for both the 3C and 5C rate, it becomes evident from the single slope at 5C that both PC811 and SC811 go through only the H1 → M and possibly M → H2 transitions due to the increased mass transfer overpotential and restricted voltage operation range. At 3C however, a plateau exists near 4 V on discharge and 4.3 V on charge and are associated with the H2 → H3 transitions which contribute an additional capacity. In contrast, this plateau is not observed

for SC811 at 3C and the capacity is subsequently lower. These observations indicate that the performance limitation and low capacity of SC811 relative to PC811 is mostly associated with the H2 → H3 transition at high voltage and is investigated further in this work.

The increased rate of capacity fade from C/2 long term cycling is associated with a steady increase in cell polarization, which is demonstrated by the respective increase or decrease in the median charge or discharge voltage during extended cycling, shown in Fig. 3d and e, which also shows an initially higher voltage difference that develops after the first formation cycles. While the cyclic voltammetry curves of PC811 shows a moderate increase in peak-to-peak width and peak broadening after 100 cycles, the redox pairs associated with the H1 → M, M → H2, and H2 → H3 transitions are still observable [13]. This is in stark contrast to cycled SC811, where only the first set of redox peaks are observed with significant peak-to-peak width and broadening, indicating the loss of electrochemically active phases [50]. Electrochemical impedance spectra (EIS) obtained before and after cycling demonstrates an immense increase in the charge transfer resistance of SC811 compared to PC811, as evidenced by the larger second semi-circle at median frequency [51].

To probe possible degradation mechanisms, cyclic voltammograms of the first 7 cycles are shown in Fig. 4a and b, using a slow scan rate of 0.1 mV/s. For both samples, anodic peaks can be observed in the first charge cycle at values above 3.8 V before settling at a lower voltage that is generally more reversible. This higher anodic peak under first charge is typically observed and is attributed to the oxidation of residual surface impurities, surface reconstruction, and subsequent formation of a CEI layer [52,53]. This can also be considered the “activation” of the NMC cathode. While PC811 has one clear anodic peak at 3.9 V, SC811 takes several cycles with lower intensity peaks before the main redox peak shifts to the expected reversible value around 3.75–3.8 V. Additionally, there is also an increased initial anodic peak for the H2 → H3 redox pair, which is not observed for PC811, suggesting that the formation of the CEI layer and electrolyte decomposition is distinctly different than PC811 and may be thicker compared to that of PC811 [54,55]. More notably is the difference between the peak-to-peak width of the redox peaks associated with the H2 → H3 transition, which occurs between ~4.0–4.2 V. While PC811 shows exceptional reversibility of the H2 → H3 transition, as evidenced by the well overlapping CV curves, SC811 shows an initially larger polarization which begins to in-

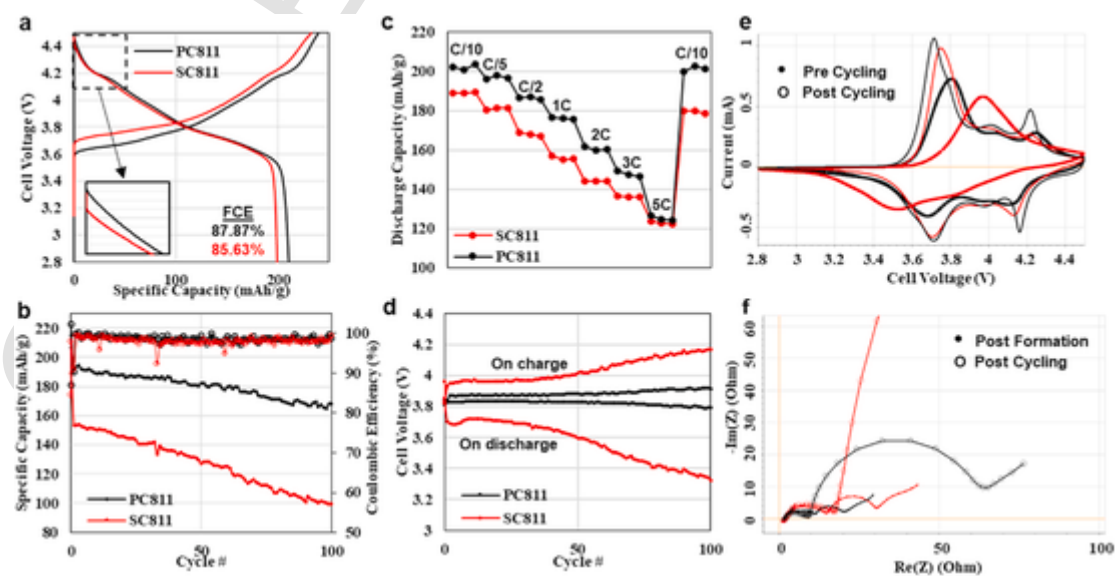


Fig. 3. Electrochemical analysis of half-cells for PC811 (black) and SC811 (red). (a) First charge/discharge cycle and first coulombic efficiency, (b) galvanostatic charge/discharge cycling at 0.5C, (c) rate performance between 2.8 and 4.5 V, (d) median charge and discharge voltage over cycling, (e) cyclic voltammetry curves before and after cycling, (f) electrochemical impedance curves before and after cycling. Inset in figure a demonstrates the higher initial potential drop of SC811 compared to PC811. (For interpretation of the references to colour in this figure legend, the reader is referred to the Web version of this article.)

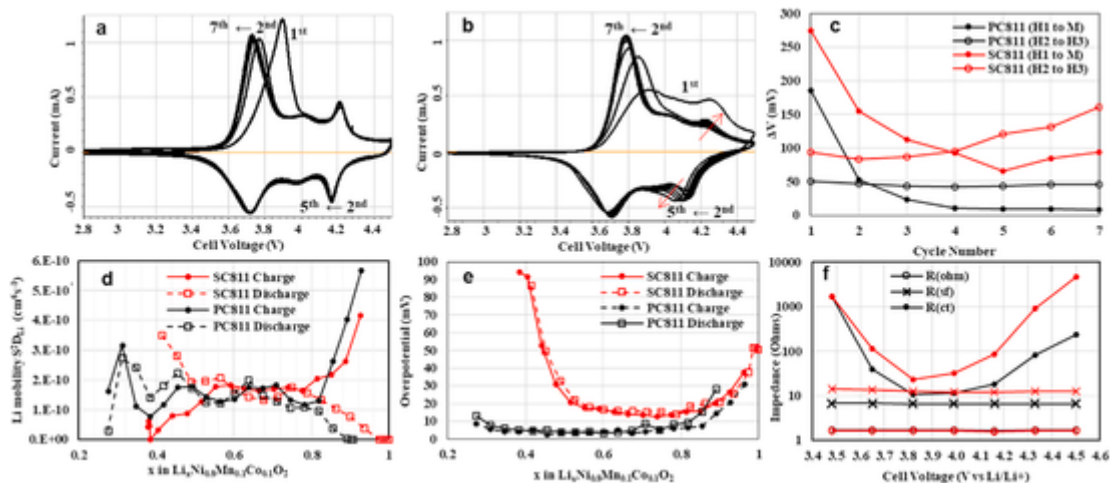


Fig. 4. Cyclic voltammograms of the initial charge/discharge and four subsequent voltammograms for (a) PC811 and (b) SC811, with (c) redox pair polarization plotted vs cycle number. (d) Lithium diffusion coefficients and (e) overpotential vs SOC determined through GITT analysis. (f) Electrochemical impedance values of PC811 and SC811 across different SOC obtained from EIS curve fitting.

crease within the first seven cycles. This is clearly shown in Fig. 4c, where the peak-to-peak width of H2→H3 redox pair grows at a significantly faster rate for SC811, demonstrating the rapid irreversibility of these transitions. By the sixth cycle, it is also observed that the H1 → M redox peaks already begin to increase in polarization, again in significant contrast to the stable peak positions of PC811 and consistent with the lower capacity and faster capacity fade of SC811 observed from extended cycling.

GITT measurements shown in Fig. 4d demonstrate no noticeable difference in the lithium diffusion coefficient between PC811 and SC811, indicating that although SC811 naturally has longer diffusion pathways, it is not considered a significant limiting factor concerning electrochemical performance. However, by analyzing the overpotential upon the application of the current pulse, a clear difference can be observed in the high SOC range [Figs. 4e and S9]. While SC811 generally shows overpotential during current application compared to PC811, a strong increase is observed after 50% delithiation, where the values for SC811 rises from a low of ~15 mV–90 mV at 40% delithiation. In comparison, the overpotential for PC811 stays well below 20 mV across the entire SOC range beyond 20% delithiation. The overpotential associated with the immediate IR drop upon current pulse is associated with phenomena occurring at fast time scales, primarily ohmic and charge transfer overpotentials [56]. By examining the EIS curves at different SOC in Fig. 4f, it is evident that while R_{sf} and R_{ohm} for PC811 and SC811 remain stable across all tested voltages, the same cannot be said for R_{ct} . While R_{ct} for both samples starts at similar values in the fully discharged state, and decreases upon initial low levels delithiation, R_{ct} for SC811 begins to increase much more rapidly than PC811 above 4.0 V. The EIS results support the observations from GITT analysis and imply that SC811 is severely limited by high impedance, particularly in the high voltage region associated with the H2 to H3 transition. Interestingly, cycling cells only to an upper voltage cutoff of 4.0 V to avoid the severe impedance rise results in similar capacity and retention between SC811 and PC811 [Fig. S11].

4.4. Surface composition at high SOC

In order to further determine mechanisms for the rapid impedance growth of SC811 samples, XPS analysis of both SC811 and PC811 samples at the high voltage of 4.5 V are conducted, examining both the surface and subsurface region. Both samples were initially subjected to two formation cycles, before charging to 4.5 V and subsequent disassembly. To analyze the subsurface components of PC811 and SC811 samples, the surface layers are removed by Ar ion polishing for 2 min at 4 kV.

The XPS of Ni 2p3 binding energies for both PC811 and SC811 samples are almost the same as shown in Figs. S12a and b. It is worth noting that the Ni^{2+} contribution has increased for both samples, which is expected due to the formation of a cation mixing/surface reconstruction layer upon charge/discharge. It is also evident that SC811 forms a thicker CEI layer; in Figs. S12c–f, Mn 2p3 and Co 2p3 peaks can only be detected after ion polishing for SC811 samples. In contrast, Mn 2p3 and Co 2p3 signals for PC811 can still be observed before polishing, indicating that the CEI layer is relatively thinner after the first formation cycles and under high SOC than for SC811.

To determine the components of the surface layer, XPS spectra of Ni 2p3, O 1s, F 1s, P 2p, and Li 1s are analyzed. As shown in Fig. 5a and d, the appearance of a peak at 857.8 eV is observed and is attributed to the decomposition of electrolyte and subsequent formation of NiF_2 surface species [57]. The XPS of Ni 2p3 binding energies of PC811 are relatively unchanged when compared to after polishing. However, the XPS of Ni 2p3 for the SC811 surface is dominated by the NiF_2 peak, suggesting higher severity of electrolyte decomposition, and confirming the development of a thicker CEI layer just after formation cycles at high charge, with lattice Ni–O contributions barely observable. The development of higher amounts of metal fluorides is also shown in the F 1s spectra in Fig. 5c and f, with noticeably higher metal fluoride signal compared to the organic fluoride signal that comes from the PVDF binder. Meanwhile, in Fig. 5b and e, the $O_{lattice}$ cannot be detected at the surface of SC811 in the charged state while it is still observable for PC811, which also indicates the difference of the CEI thickness. There is a new peak, representing the organic compounds, can be observed in the spectra of O 1s, at the position of 533 eV and is likely due to some residual electrolyte [58].

Examination of the Li 1s and P 2p, and Li 1s in Fig. 5g and h further reveals extensive formation of CEI surface species. A significantly higher peak in the Li 1s and P 2p spectra related to LiF and $Li_xPO_yF_z$ is observed for SC811 compared to PC811, respectively. These residual surface species are well documented to be highly ionically resistive [59], and thus, with more surface species forming on the surface for SC811, the impedance and polarization growth of SC811 samples gradually increase during cycling, consistent with CV and EIS analysis. The difference in the CEI growth rate must be attributed to the higher surface reactivity of SC811, due to the known higher energy of the (012) facet compared to other possible facets and demonstrated by the higher O_{active} contribution.

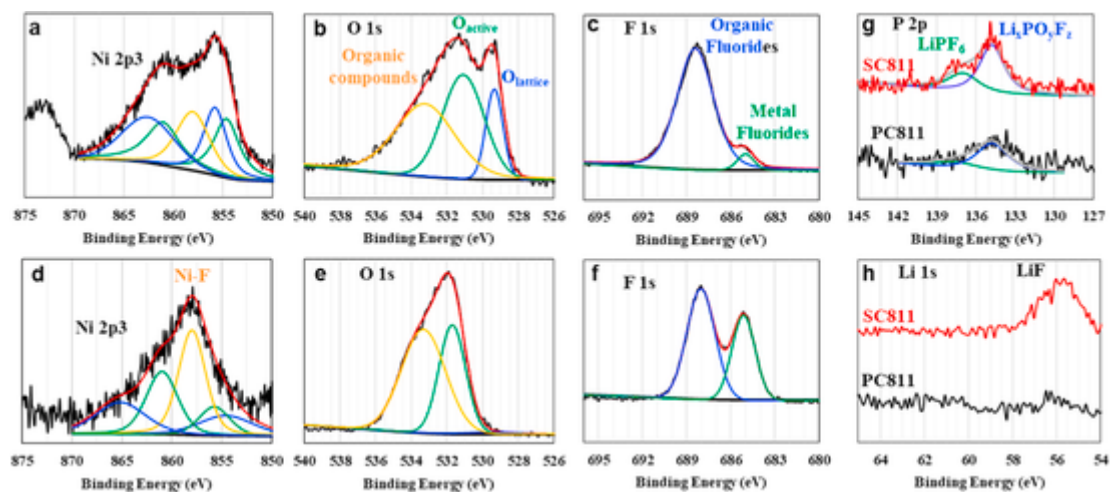


Fig. 5. Ni 2p₃, O 1s, and F 1s XPS spectra from (a–c) PC811 and (d–f) SC811 electrode surfaces from disassembled half-cells after holding at 4.5 V. (g,h) P 2p and Li 1s XPS spectra the charged electrodes.

4.5. Structural integrity vs SOC

Besides the thick CEI layer growth, intragranular cracking is also a possible reason for the fast-increasing impedance of SC811 samples, due to the generation of additional surfaces for electrolyte penetration and possible electrical disconnection. As shown in Figs. 6, S15, and S16, cracks in both PC811 and SC811 samples occur at voltages at 4.3 V and higher and are analyzed by SEM. When the voltage is less than 4.0 V, little to no cracks were observed for both samples [Fig. 6a, b, e, and f]. Once the voltage reaches 4.3V, obvious cracks can be observed on the PC811 samples in the form of intergranular cracks along grain boundaries, as shown in Fig. 6c, with most of the cracks being recoverable upon discharge as shown in Fig. 6a. For SC811 samples, rather than intergranular cracking, intragranular cracking and planar gliding can be observed in Fig. 6g and h and are assumed to be mainly along the weaker (003) basal plane, which becomes more mechanically compromised at higher levels of delithiation [60,61]. The retaining effects of planar gliding was observed for several crystals after lithiation [Fig. 6e]. Overall, it is demonstrated that at a high voltage state, significant amounts of intergranular in the case of polycrystalline NMC811, or intragranular cracking in the case of single-crystalline NMC811, can occur even just after the first formation cycle. No cracking of the individual primary particles is observed for the polycrystalline samples, as slip planes are held in place due to the neighboring grain boundary network

[61,62]. The long-term impacts of these contrasting mechanisms differ from each other; intergranular cracking is limited to only the grain boundaries and would expectedly crack along the same grain boundaries during cycling, eventually leading to microcrack propagation. In contrast, intragranular cracking or planar gliding affects the (003) basal plane, which can occur multiple times in different locations along a single crystal cathode particle, running parallel to each other as observed in Fig. 6e–h. With each cycle, numerous new surfaces are possibly generated and exposed to electrolyte penetration and surface-initiated reactions. In addition, these defects are produced by strain within the crystal lattice at high voltage, which likely affects the lithium intercalation process and resulting in the high impedance at moderate levels of delithiation observed in Fig. 4. This contrast between intragranular and intergranular fracture is likely a defining feature that contributes to the rapid impedance growth and fast capacity fade for SC811 observed from electrochemical analysis.

The previously proposed mechanisms of CEI layer growth and intragranular cracking on PC811 and SC811 samples are further confirmed by HRTEM. PC811 and SC811 samples charged to 4.5 V after the first formation cycle are examined in Fig. 7. From Fig. 7a and b, it was observed that the CEI layer for SC811 samples is noticeably thicker (~5 nm) than that of PC811 samples (~1 nm), consistent with conclusions drawn from XPS results and would result in the poorer electrochemical performance of SC811 compared to PC811. Meanwhile, in

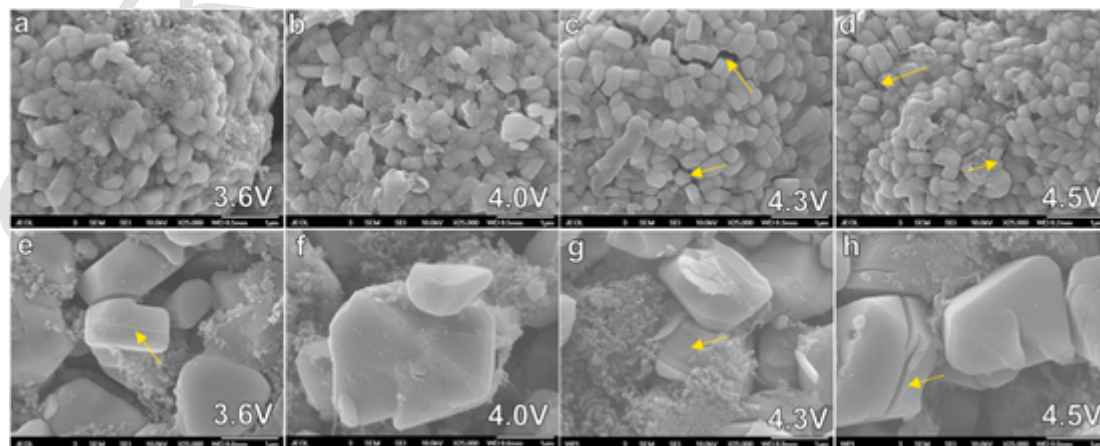


Fig. 6. SEM images of (a–d) PC811 and (e–h) SC811 electrodes retrieved from disassembled cells after holding at various upper cutoff voltage. Intragranular cracks in PC811 can be observed to being at 4.3 V, whereas gliding planes or intergranular cracks can be clearly seen spanning the entire length of the single crystalline grains. Note that all cells were subjected to 1 formation cycle between 2.8 and 4.5 V before holding at target voltage.

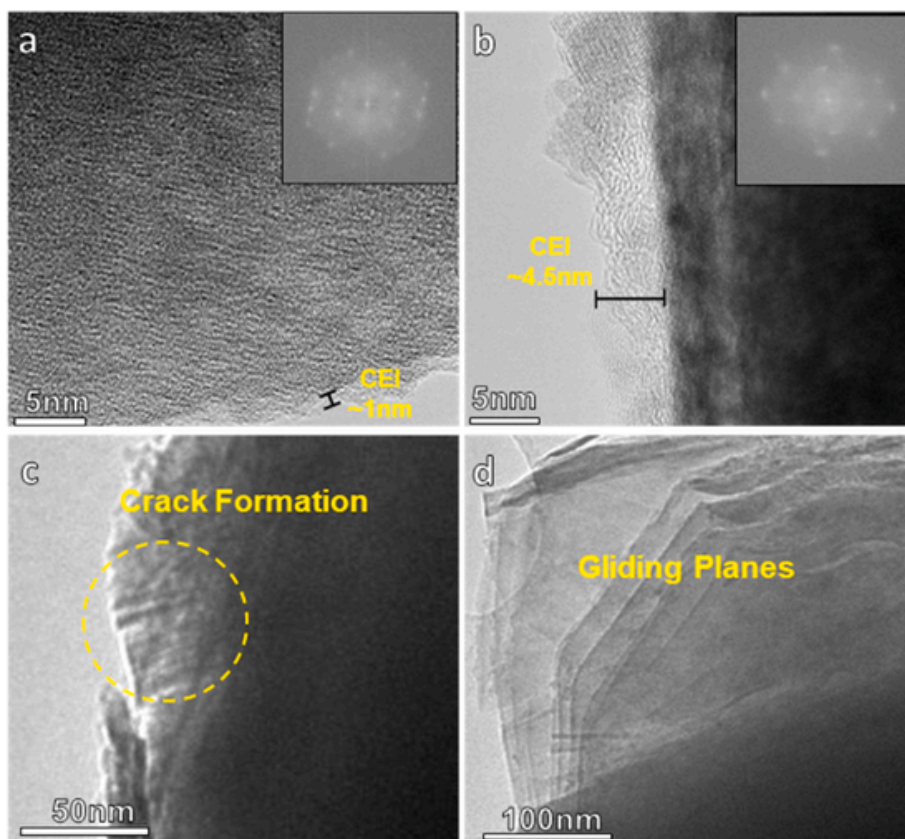


Fig. 7. TEM images of (a) PC811 and (b–d) SC811 taken from electrodes charged and held at 4.5 V after one formation cycle. Surface reconstruction is observed for both samples based on the FFT patterns in the inset. The occurrence of intragranular fracture and planar gliding is evident for SC811.

Fig. 7c and d, evidence of intragranular cracking and planar gliding is observed. While the severity of planar gliding observed in Fig. 7d is likely exacerbated by TEM sample preparation techniques (ultrasonic dispersion in NMP and ethanol), it is further indication of the anisotropic structural instability of Ni-rich single crystal cathodes, which occurs within the first cycle during high voltage regions and results in further exposure to electrolyte penetration and expected detrimental surface reactivity.

5. Conclusion

In summary, a facile molten salt assisted synthesis approach towards single crystalline NMC811 is demonstrated. The addition of excess lithium and high temperature was necessary for crystal growth, with the use of alkali sulfate minimizing agglomeration. The resulting cathode material composed of 1–2 μm crystals with significant octahedral faceting exhibits excellent crystallinity, surface nickel valence, and minimal impurities. However, the higher reactivity of the surface due to the dominant (012) facets compared to its polycrystalline counterpart leads to the formation of a thick CEI layer within the first few formation cycles which dramatically increases the charge transfer resistance as demonstrated by the large polarization drops during GITT analysis and probed using CV and EIS techniques. Lithium diffusion was not found to be a significant limiting factor. In addition, the single crystal cathode is susceptible to intragranular cracking, especially within the high voltage region above 4.2 V associated with the H2 \rightarrow H3 transition, exhibiting significant irreversibility and increasing polarization again within just the first few cycles. The intragranular cracking is preceded by planar gliding of the (003) basal planes, which can occur across the entire length of the NMC particle and expose new surfaces to electrolyte with each cycle. The irreversibility and capacity loss mainly associated with the high voltage region may also be influenced by surface/bulk strain

issues limiting proper lithium intercalation and rendering significant fractions of the material inactive, which has been proposed as a general limitation of Ni-rich cathodes and would require further study [63].

In order to develop high performing single-crystalline Ni-rich cathodes, these obstacles must be overcome, with the use of dopants or coatings as a possible solution, a variety of which is already demonstrated for polycrystalline morphologies [64–68]. Future work should focus on coating selection and methodology, and/or dopant selection and concentration with an objective towards stabilizing the single-crystal cathode surface. Modification approaches must achieve the formation of a thinner and stable CEI as well as better H2 \rightarrow H3 reversibility. Recent work by Fan et al. utilized a coating of a NASICON-type $\text{Li}_{1.4}\text{Y}_4\text{Ti}_{1.6}(\text{PO}_4)_3$ onto single crystal Ni-rich cathode powder to form a both protective and ionic conductive network with moderate Ti-doping, which is a promising approach [69]. The utilization of other types of dominant facets should also be studied, although other works imply that the (012) facet is the most suitable for high-capacity Ni-rich crystals [30]. This work demonstrates some limitations of single crystalline morphology of Ni-rich cathodes and provides guidance towards improvement and the development of Ni-rich cathodes for next generation lithium-ion batteries.

CRediT authorship contribution statement

Luqman Azhari : Conceptualization, Methodology, Visualization, Investigation, Validation, Writing – original draft. **Zifei Meng** : Investigation, Writing – original draft. **Zhenzhen Yang** : Investigation. **Guanhui Gao** : Investigation. **Yimo Han** : Investigation. **Yan Wang** : Conceptualization, Methodology, Supervision, Writing – review & editing.

Declaration of competing interest

The authors declare the following financial interests/personal relationships which may be considered as potential competing interests: Luqman Azhari reports financial support was provided by Ford Motor Company through the Ford University Research Program (URP). Luqman Azhari reports a relationship with Ford Motor Company that includes: funding grants.

Data availability

Data will be made available on request.

Acknowledgements

This work was made possible under the financial support of the Ford Motor Company University Research Project. BET and PSD analysis was conducted with assistance from Ascend Elements. XPS analysis was conducted by Dr. Yang at the Chemical Science and Engineering Division at Argonne National Lab. TEM EDS mapping was conducted with assistance by Dr. Gao and Dr. Han at the Rice Electron Microscopy Center at Rice University. Additional TEM analysis was conducted with assistance from Dr. Wentao Liang from the Kostas Advanced Nano-Characterization Facility (KANCF), Northeastern University Innovation Campus of Burlington Massachusetts (ICBM).

Appendix A. Supplementary data

Supplementary data to this article can be found online at <https://doi.org/10.1016/j.jpowsour.2022.231963>.

References

- Y. Ding, Z.P. Cano, A. Yu, J. Lu, Z. Chen, Automotive Li-ion batteries: current status and future perspectives, *Electrochem. Energy Rev.* 2 (2019) 1–28.
- S.W.D. Gourley, T. Or, Z. Chen, Breaking free from cobalt reliance in lithium-ion batteries, *iScience* 23 (2020) 101505.
- N. Muralidharan, et al., Next-generation cobalt-free cathodes – a prospective solution to the battery industry's cobalt problem, *Adv. Energy Mater.* 12 (2022) <https://doi.org/10.1002/aenm.202103050>, Preprint at.
- Y. Xia, J. Zheng, C. Wang, M. Gu, Designing principle for Ni-rich cathode materials with high energy density for practical applications, *Nano Energy* 49 (2018) 434–452.
- J. Duan, et al., Building safe lithium-ion batteries for electric vehicles: a review, *Electrochem. Energy Rev.* 3 (2020) <https://doi.org/10.1007/s41918-019-00060-4>, Preprint at.
- X. Wang, Y. Ding, Y. Deng, Z. Chen, Ni-Rich/Co-Poor layered cathode for automotive Li-ion batteries: promises and challenges, *Adv. Energy Mater.* 10 (2020) 1903864.
- J. Kim, et al., Prospect and reality of Ni-rich cathode for commercialization, *Adv. Energy Mater.* 8 (2018) 1702028.
- Q. Gan, et al., Revealing mechanism of Li₃PO₄ coating suppressed surface oxygen release for commercial Ni-rich layered cathodes, *ACS Appl. Energy Mater.* 3 (2020) 7445–7455.
- C. Yang, et al., Bulk and surface degradation in layered Ni-rich cathode for Li ions batteries: defect proliferation via chain reaction mechanism, *Energy Storage Mater.* 35 (2021) 62–69.
- H.-H. Ryu, G.-T. Park, C.S. Yoon, Y.-K. Sun, Microstructural degradation of Ni-rich Li[Ni_xCo_yMn_{1-x-y}]O₂ cathodes during accelerated calendar aging, *Small* 14 (2018) 1803179.
- S. Klein, et al., Demonstrating apparently inconspicuous but sensitive impacts on the rollover failure of lithium-ion batteries at a high voltage, *ACS Appl. Mater. Interfaces* 13 (2021) 57241–57251.
- J. Kasnatscheew, et al., Changing established belief on capacity fade mechanisms: thorough investigation of LiNi_{1/3}Co_{1/3}Mn_{1/3}O₂ (NCM111) under high voltage conditions, *J. Phys. Chem. C* 121 (2017) 1521–1529.
- K. Märker, P.J. Reeves, C. Xu, K.J. Griffith, C.P. Grey, Evolution of structure and lithium dynamics in LiNi_{0.8}Mn_{0.1}Co_{0.1}O₂ (NMC811) cathodes during electrochemical cycling, *Chem. Mater.* 31 (2019) 2545–2554.
- B. You, et al., Research progress of single-crystal nickel-rich cathode materials for lithium ion batteries, *Small Methods* 5 (2021) 2100234.
- W. Zeng, et al., Single-crystal high-nickel layered cathodes for lithium-ion batteries: advantages, mechanism, challenges and approaches, *Curr. Opin. Electrochem.* 31 (2022) 100831.
- J. Langdon, A. Manthiram, A perspective on single-crystal layered oxide cathodes for lithium-ion batteries, *Energy Storage Mater.* 37 (2021) 143–160.
- K.-J. Park, et al., Degradation mechanism of Ni-enriched NCA cathode for lithium batteries: are microcracks really critical? *ACS Energy Lett.* 4 (2019) 1394–1400.
- P. Teichert, G.G. Eshetu, H. Jahnke, E. Figgemeier, Degradation and aging routes of Ni-rich cathode based Li-ion batteries, *Batteries* 6 (2020) 8.
- W. Bao, et al., Simultaneous enhancement of interfacial stability and kinetics of single-crystal LiNi_{0.6}Mn_{0.2}Co_{0.2}O₂ through optimized surface coating and doping, *Nano Lett.* 20 (2020) 8832–8840.
- J. Li, et al., Comparison of single crystal and polycrystalline LiNi_{0.5}Mn_{0.3}Co_{0.2}O₂ positive electrode materials for high voltage Li-ion cells, *J. Electrochem. Soc.* 164 (2017) A1534–A1544.
- E. Trevisanello, R. Ruess, G. Conforto, F.H. Richter, Janek, J. Polycrystalline and single crystalline NCM cathode materials—quantifying particle cracking, active surface area, and lithium diffusion, *Adv. Energy Mater.* 11 (2021) 2003400.
- G. Qian, et al., Single-crystal nickel-rich layered-oxide battery cathode materials: synthesis, electrochemistry, and intra-granular fracture, *Energy Storage Mater.* 27 (2020) 140–149.
- Y. Kim, Lithium nickel cobalt manganese oxide synthesized using alkali chloride flux: morphology and performance as a cathode material for lithium ion batteries, *ACS Appl. Mater. Interfaces* 4 (2012) 2329–2333.
- T. Kimijima, N. Zetsu, K. Teshima, Growth manner of octahedral-shaped Li(Ni_{1/3}Co_{1/3}Mn_{1/3})O₂ single crystals in molten Na₂SO₄, *Cryst. Growth Des.* 16 (2016) 2618–2623.
- H. Li, J. Li, X. Ma, J.R. Dahn, Synthesis of single crystal LiNi_{0.6}Mn_{0.2}Co_{0.2}O₂ with enhanced electrochemical performance for lithium ion batteries, *J. Electrochem. Soc.* 165 (2018) A1038–A1045.
- E.J. Cheng, et al., Mechanical and physical properties of LiNi_{0.33}Mn_{0.33}Co_{0.33}O₂ (NMC), *J. Eur. Ceram. Soc.* 37 (2017) 3213–3217.
- L. Zheng, J.C. Bennett, M.N. Obrovac, All-dry synthesis of single crystal NMC cathode materials for Li-ion batteries, *J. Electrochem. Soc.* 167 (2020) 130536.
- X. Ma, et al., A universal etching method for synthesizing high-performance single crystal cathode materials, *Nano Energy* 87 (2021) 106194.
- G. Qian, et al., Temperature-swing synthesis of large-size single-crystal LiNi_{0.6}Mn_{0.2}Co_{0.2}O₂ cathode materials, *J. Electrochem. Soc.* 168 (2021) 010534.
- J. Zhu, G. Chen, Single-crystal based studies for correlating the properties and high-voltage performance of Li[Ni_xMn_yCo_{1-x-y}]O₂ cathodes, *J. Mater. Chem.* 7 (2019) 5463–5474.
- H. Li, et al., Synthesis of single crystal LiNi_{0.88}Co_{0.09}Al_{0.03}O₂ with a two-step lithiation method, *J. Electrochem. Soc.* 166 (2019) A1956–A1963.
- J. Li, et al., Comparison of single crystal and polycrystalline LiNi_{0.5}Mn_{0.3}Co_{0.2}O₂ positive electrode materials for high voltage Li-ion cells, *J. Electrochem. Soc.* 164 (2017) A1534–A1544.
- S. Klein, et al., Prospects and limitations of single-crystal cathode materials to overcome cross-talk phenomena in high-voltage lithium ion cells, *J. Mater. Chem.* 9 (2021) 7546–7555.
- W. Zhao, et al., Assessing long-term cycling stability of single-crystal versus polycrystalline nickel-rich NCM in pouch cells with 6 mAh cm⁻² electrodes, *Small* 18 (2022) 2107357.
- H. Ronduda, et al., On the sensitivity of the Ni-rich layered cathode materials for Li-ion batteries to the different calcination conditions, *Nanomaterials* 10 (2020) 2018.
- C. Yang, Superior cycle stability of single crystal nickel-rich layered oxides with micron-scale grain size as cathode material for lithium ion batteries, *Int. J. Electrochem. Sci.* (2020) 5031–5041, <https://doi.org/10.20964/2020.06.03>.
- L. Azhari, R. Arsenault, G. Gao, Y. Wang, Modified nickel-rich cathodes via conformal nanoparticle coating of precursors using a single reactor process, *ACS Appl. Energy Mater.* 4 (2021) 14618–14627.
- FactSage FTSalt, FACT Salt Phase Diagrams, 2022.
- X. Xiao, F. Hayashi, K. Yubuta, A. Selloni, K. Teshima, Effects of alkali cations and sulfate/chloride anions on the flux growth of {001}-Faceted β-Li₂TiO₃ crystals, *Cryst. Growth Des.* 17 (2017) 1118–1124.
- K.H. Yoon, Y.-S. Cho, D.-H. Lee, D.-H. Kang, Powder characteristics of Pb(Mg_{1/3}Nb_{2/3})O₃ prepared by molten salt synthesis, *J. Am. Ceram. Soc.* 76 (1993) 1373–1376.
- A.J. Cortese, et al., Oxygen anion solubility as a factor in molten flux crystal growth, synthesis, and characterization of four new reduced lanthanide molybdenum oxides: Ce_{4.918(3)}Mo₃O₁₆, Pr_{4.880(3)}Mo₃O₁₆, Nd_{4.910(3)}Mo₃O₁₆, and Sm_{4.952(3)}Mo₃O₁₆, *Cryst. Growth Des.* 16 (2016) 4225–4231.
- F. Zhang, et al., Surface regulation enables high stability of single-crystal lithium-ion cathodes at high voltage, *Nat. Commun.* 11 (2020) 3050.
- Z. Zheng, et al., High performance cathode recovery from different electric vehicle recycling streams, *ACS Sustain. Chem. Eng.* 6 (2018) 13977–13982.
- X. Zhang, et al., Minimization of the cation mixing in Li_{1+x}(NMC)1-xO₂ as cathode material, *J. Power Sources* 195 (2010) 1292–1301.
- R. Zhang, et al., Understanding fundamental effects of Cu impurity in different forms for recovered LiNi_{0.6}Co_{0.2}Mn_{0.2}O₂ cathode materials, *Nano Energy* 78 (2020) 105214.
- Z. Fu, J. Hu, W. Hu, S. Yang, Y. Luo, Quantitative analysis of Ni₂₊/Ni₃₊ in Li[Ni_xMn_yCo_z]O₂ cathode materials: non-linear least-squares fitting of XPS spectra, *Appl. Surf. Sci.* 441 (2018) 1048–1056.
- N.-H. Yeh, et al., Controlling Ni²⁺ from the surface to the bulk by a new cathode electrolyte interphase formation on a Ni-rich layered cathode in high-safe and high-energy-density lithium-ion batteries, *ACS Appl. Mater. Interfaces* 13 (2021) 7355–7369.
- C. Lv, et al., Revealing the degradation mechanism of Ni-rich cathode materials after ambient storage and related regeneration method, *J. Mater. Chem.* 9 (2021) 3995–4006.

- [49] T. Wang, et al., Tuning the Li/Ni disorder of the NMC811 cathode by thermally driven competition between lattice ordering and structure decomposition, *J. Phys. Chem. C* 124 (2020) 5600–5607.
- [50] L. Liang, et al., Nasicon-type surface functional modification in core-shell $\text{LiNi}_{0.5}\text{Mn}_{0.3}\text{Co}_{0.2}\text{O}_2 @ \text{NaTi}_2(\text{PO}_4)_3$ cathode enhances its high-voltage cycling stability and rate capacity toward Li-ion batteries, *ACS Appl. Mater. Interfaces* 10 (2018) 5498–5510.
- [51] L. Saunders, J. Wang, U. Stimming, Evaluating single-crystal and polycrystalline NMC811 electrodes in lithium-ion cells via non-destructive EIS alone, *J. Appl. Electrochem.* (2022), <https://doi.org/10.1007/s10800-022-01713-x>.
- [52] R. Robert, C. Bünzli, E.J. Berg, P. Novák, Activation mechanism of $\text{LiNi}_{0.80}\text{Co}_{0.15}\text{Al}_{0.05}\text{O}_2$: surface and bulk operando electrochemical, differential electrochemical mass spectrometry, and X-ray diffraction analyses, *Chem. Mater.* 27 (2015) 526–536.
- [53] A. Grenier, et al., Reaction heterogeneity in $\text{LiNi}_{0.8}\text{Co}_{0.15}\text{Al}_{0.05}\text{O}_2$ induced by surface layer, *Chem. Mater.* 29 (2017) 7345–7352.
- [54] J. Jeyakumar, Y.-S. Wu, S.-H. Wu, R. Jose, C.-C. Yang, Surface-modified quaternary layered Ni-rich cathode materials by Li_2ZrO_3 for improved electrochemical performance for high-power Li-ion batteries, *ACS Appl. Energy Mater.* 5 (2022) 4796–4807.
- [55] R. Ma, et al., Tuning cobalt-free nickel-rich layered $\text{LiNi}_{0.9}\text{Mn}_{0.1}\text{O}_2$ cathode material for lithium-ion batteries, *Chemelectrochem* 7 (2020) 2637–2642.
- [56] Y. Chen, et al., Revealing the rate-limiting electrode of lithium batteries at high rates and mass loadings, *SSRN Electron. J.* (2022), <https://doi.org/10.2139/ssrn.4117009>.
- [57] Y.-M. Lee, et al., Interfacial origin of performance improvement and fade for 4.6 V $\text{LiNi}_{0.5}\text{Co}_{0.2}\text{Mn}_{0.3}\text{O}_2$ battery cathodes, *J. Phys. Chem. C* 118 (2014) 10631–10639.
- [58] K. Edström, T. Gustafsson, J.O. Thomas, The cathode–electrolyte interface in the Li-ion battery, *Electrochim. Acta* 50 (2004) 397–403.
- [59] A. Soloy, et al., Effect of particle size on $\text{LiNi}_{0.6}\text{Mn}_{0.2}\text{Co}_{0.2}\text{O}_2$ layered oxide performance in Li-ion batteries, *ACS Appl. Energy Mater.* 5 (2022) 5617–5632.
- [60] Y. Bi, et al., Reversible planar gliding and microcracking in a single-crystalline Ni-rich cathode, *Science* 370 (1979) 1313–1317 2020.
- [61] J.C. Stallard, et al., Effect of lithiation upon the shear strength of NMC811 single crystals, *J. Electrochem. Soc.* 169 (2022) 040511.
- [62] J.C. Stallard, et al., Mechanical properties of cathode materials for lithium-ion batteries, *Joule* 6 (2022) 984–1007.
- [63] C. Xu, et al., Bulk fatigue induced by surface reconstruction in layered Ni-rich cathodes for Li-ion batteries, *Nat. Mater.* 20 (2021) 84–92.
- [64] K.-J. Park, et al., Improved cycling stability of $\text{Li}[\text{Ni}_{0.90}\text{Co}_{0.05}\text{Mn}_{0.05}]\text{O}_2$ through microstructure modification by boron doping for Li-ion batteries, *Adv. Energy Mater.* 8 (2018) 1801202.
- [65] Y. Gao, J. Park, X. Liang, Comprehensive study of Al- and Zr-modified $\text{LiNi}_{0.8}\text{Mn}_{0.1}\text{Co}_{0.1}\text{O}_2$ through synergy of coating and doping, *ACS Appl. Energy Mater.* 3 (2020) 8978–8987.
- [66] J.D. Steiner, et al., Targeted surface doping with reversible local environment improves oxygen stability at the electrochemical interfaces of nickel-rich cathode materials, *ACS Appl. Mater. Interfaces* 11 (2019) 37885–37891.
- [67] H. Li, et al., Stabilizing nickel-rich layered oxide cathodes by magnesium doping for rechargeable lithium-ion batteries, *Chem. Sci.* 10 (2019) 1374–1379.
- [68] B. Han, et al., From coating to dopant: how the transition metal composition affects alumina coatings on Ni-rich cathodes, *ACS Appl. Mater. Interfaces* 9 (2017) 41291–41302.
- [69] X. Fan, et al., In situ inorganic conductive network formation in high-voltage single-crystal Ni-rich cathodes, *Nat. Commun.* 12 (2021) 5320.